Journal of Alloys and Metallurgical Systems 2 (2023) 100011

Contents lists available at ScienceDirect

Journal of Alloys and Metallurgical Systems

journal homepage: www.journals.elsevier.com/journal-of-alloys-and-metallurgical-systems

Co-segregation of Y and Zr in W-Cr-Y-Zr alloys: First-principles modeling at finite temperature and application to SMART materials

Damian Sobieraj[a,*], Jan S. Wróbel[a], Mark R. Gilbert[b], Krzysztof J. Kurzydłowski[a,c], Duc Nguyen-Manh[b,*]

[a] Faculty of Materials Science and Engineering, Warsaw University of Technology, ul. Wołoska 141, 02-507 Warsaw, Poland
[b] United Kingdom Atomic Energy Authority, Culham Centre for Fusion Energy, Culham Science Centre, Abingdon, Oxon OX14 3DB, UK
[c] Faculty of Mechanical Engineering, Bialystok University of Technology, ul. Wiejska 45, 15-351 Bialystok, Poland

ARTICLE INFO

PACS:
0000
1111

2000 MSC:
0000
1111

Keywords:
Nuclear reactor materials
Metals and alloys
Atomic scale structure
Enthalpy
Computer simulations
Thermodynamic modeling

ABSTRACT

Spinodal phase separation in SMART (Self-passivating Metal Alloys with Reduced Thermo-oxidation) materials based on binary W-Cr with alloying elements Y and Zr is systematically investigated by a combination of Density Functional Theory with Cluster Expansion Hamiltonian and large-scale Monte Carlo simulations with thermodynamic integration. Comparing alloys of Zr with those of Y in ternary compositions with W and Cr, it is shown that there is a significant difference in the average short-range order between W and Zr, which changes from positive to negative from 500 K to higher temperatures in $W_{70}Cr_{29}Zr_1$ alloys compared with the positive SRO (Short-Range Order) between W and Y in $W_{70}Cr_{29}Y_1$ alloys at all temperatures. This change, however, does not affect the segregation behavior between W and Cr in the whole range of temperature between these alloys. Importantly, it is found that co-segregation of Y and Zr due to the negative SRO between them, in $W_{70}Cr_{29}Y_{0.5}Zr_{0.5}$ and $W_{70}Cr_{28}Y_1Zr_1$ considered alloys, increases the W-Cr positive SRO closer to the binary $W_{70}Cr_{30}$. Our modeling results reveal a significant impact on spinodal phase segregation of W and Cr in designing SMART materials for DEMO devices of future fusion power plants. Findings from recent experimental studies validate the modeling results, particularly the high-temperature behavior of the W-Cr-Zr alloys and the microstructure evolution of the W-Cr-Y-Zr alloys. The results provide a fundamental understanding of the radiation resistance phenomena observed in recent experiments on neutron-irradiated self-passivating alloys.

1. Introduction

Tungsten (W) represents one of the important baseline materials for in-vessel components in the demonstration fusion power plant (DEMO) design activities [1]. Due to its attractive thermo-physical properties, such as high melting point, high strength, low coefficient of thermal expansion, low vapor pressure, and high thermal conductivity, W-based materials remain among the priorities of fusion research and development. Pure W, however, has some drawbacks, such as the high brittle-to-ductile transition temperature (DBTT) (for sintered W, it lies in the range 400–600°C) and recrystallization-induced loss of strength which occurs at a temperature at above 1100°C. Another drawback of W is its poor oxidation resistance resulting in fast oxidation at temperatures above 500°C and significant oxide sublimation above 900°C [2]. Therefore, the use of pure W represents a potential safety risk in case of a loss-of-coolant accident (LOCA) with simultaneous air ingress into the vacuum vessel (loss-of-vacuum accident [LOVA]). In such a situation, the first wall W oxidizes, forming volatile radioactive WO_3 with the potential release of significant amounts of highly activated species"[3]. The radioactive W oxide can be mobilized to the environment at a rate of 10–150 kg per hour [4].

Self-passivating Metal Alloys with Reduced Thermo-oxidation (SMART) were originally proposed and developed by Koch and Bolt [5]. These alloys change their properties depending on the environment. During regular plasma operation, the lighter alloying elements such as chromium (Cr), Yttrium (Y), or Zirconium (Zr) will be more easily sputtered by plasma particles, leaving most of the pure W surface facing the plasma and having all aforementioned advantages of pure W. When exposed to air at high temperatures, Cr can form a protective chromium oxide (Cr_2O_3) scale on the surface of W-Cr-based alloys, thus preventing

* Corresponding authors.
E-mail addresses: damian.sobieraj.dokt@pw.edu.pl (D. Sobieraj), duc.nguyen@ukaea.uk (D. Nguyen-Manh).

https://doi.org/10.1016/j.jalmes.2023.100011
Received 13 March 2023; Received in revised form 14 May 2023; Accepted 15 May 2023
Available online 16 May 2023

the further oxidation of W [6]. Most recently, it has been found that the bending strength in SMART alloys W-Cr-Y has increased under neutron irradiation, and the increase is remarkably higher at the highest irradiation temperature T_{irr} = 1000°C. The microstructure analysis showed that under irradiation, the single-phase matrix at high temperature undergoes a spinodal-like decomposition resulting in a two-phase ultrafine-grained microstructure [7]. An excellent anti-oxidant performance and microstructure evolution in the W-Cr-Zr alloy powders prepared through mechanical alloying in different modes were investigated in [8]. SMART W-Cr-Y-Zr alloys of different compositions were manufactured, and their microstructure was analyzed after heat treatment at 1555°C and oxidation screening test [9]. According to the results of that study, the oxidation behavior of W-10Cr-0.5Y-0.5Zr in dry air may represent the best system in comparison with W-10Cr-0.5Y and W-10Cr-0.5Zr alloys.

Atomistic modeling based on combining first-principles calculations with constructing the Cluster Expansion (CE) Hamiltonian for large-scale Monte-Carlo simulations has been developed for irradiation tolerant refractory W alloys for composition stability and segregation behavior predictions [10–12]. The development has also been applied to the W-Cr-Y alloys and integrated well with experimental research activities to support the industrial scale-up of SMART alloy development for fusion applications [13,14]. It predicts the maintenance of the spinodal phase decomposition between W and Cr as a result of Y alloying due to the positive short-range order of not only W-Cr but also W-Y and Cr-Y pairs as a function of temperature. The prediction is in excellent agreement with the recent experimental observations of chemical spinodal boundaries in microstructure evolution in these SMART materials irradiated between 600°C and 1000°C [7].

The main purpose of this present work is to extend our previous modeling studies to SMART alloys containing Zr. In Section 2, the Density Functional Theory (DFT) calculations for creating a first-principles database for the quaternary W-Cr-Y-Zr system as well as the corresponding Effective Cluster Interactions (ECIs), are discussed. In addition, nuclear inventory calculations for the transmutation and activation of these alloys are also presented. In Section 3, the composition stability of SMART materials with separated Zr and Y alloying elements is investigated and compared. In Section 4, the analysis of chemical short-range ordering for the quaternary system is discussed as a function of composition and temperature. The free energy calculations in W-Cr-Y-Zr alloys are performed systematically in Section 4 as well. In Section 5, the discussion on the application of the model to a wider range of compositions and experimental validation of modeling results are presented. In Section 6, the conclusions of our study are summarized.

2. Transmutation and activation simulations

In the previous work [13], nuclear responses, measured by transmutation and activation rates, were calculated for pure elements being considered in the development of SMART alloys. Here, we repeat those calculations for the four alloy compositions $W_{70}Cr_{30}$, $W_{70}Cr_{29}Zr_1$, $W_{70}Cr_{29}Y_1$ and $W_{70}Cr_{28}Y_1Zr_1$, where the subscripts refer to the atomic % of each element in the alloy. Fig. 1 shows the predicted evolution in the composition of the four different alloys during exposure to a 2-year continuous (full-power) irradiation under the conditions expected for the first wall of a typical concept design for the European demonstration fusion power plant (EU-DEMO). The neutron flux-energy-spectrum used in the calculations corresponds to the equatorial outboard first wall of the conceptual design of a European demonstration fusion power plant [15]. Two years of continuous full power operation is equivalent, in terms of total neutron fluence, to the five years of pulsed operation planned for the first phase of EU-DEMO operation, after which the first wall components will be replaced [16–20]. The inventory code FISPACT-II [21] was used with TENDL-2019 [22] nuclear data to predict change in composition due to the transmutation, which is shown in the plots by the growth in concentration (defined in units of atomic parts per million or appm) of elements different from those in the original alloy composition – the concentration of those original elements are largely unchanged, and so are represented by near-horizontal lines in the plots. FISPACT-II can also evolve compositions after irradiation during decay cooling and hence derive the total activity of the material at each time based on the half-lives of the decaying radionuclides in the composition. Fig. 2 shows the results of this activity evolution, measured in Becquerels per kg of each alloy, for 1000 years after the end of the 2-year exposure.

3. Computational methodology for atomistic simulations

3.1. DFT computational details and cluster expansion formalism

DFT calculations were performed using Vienna Ab-initio Simulation Package (VASP) together with the projector augmented wave (PAW) method [23–26]. The generalized gradient approximation (GGA-PBE) was used for exchange and correlation functional [27]. The acceleration of DFT calculations was achieved by using PAW potentials without semi-core p electron contribution [12]. Since the difference between values of the enthalpy of mixing of anti-ferromagnetic and non-magnetic Cr-rich structures was small, the magnetism was not taken into consideration in the present study.

The Monkhorst-Pack mesh [28] of k points in the Brillouin zone, with k-mesh spacing of 0.15 $Å^{-1}$ was used to calculate the total energies. For a 2-atom bcc cubic cell, this corresponds to $14 \times 14 \times 14$ k-point mesh. The plane-wave cutoff energy value was set to 400 eV for the carried calculations. The force components were relaxed to 10^{-3} eV/Åand the total energy convergence criterion was set to 10^{-6} eV/cell.

DFT and CE methods were used to calculate the enthalpies of mixing of all bcc structures in the developed Cr-W-Y-Zr system. The enthalpy of mixing of an alloy can also be calculated using the Cluster Expansion method[12,13]:

$$\Delta H^{bcc}_{mixCE}(\vec{\sigma}) = \sum_{\omega} m_{\omega} J_{\omega} \langle \Gamma_{\omega'}(\vec{\sigma}) \rangle_{\omega}, \tag{1}$$

where the summation is performed over all clusters ω that are distinct under group symmetry operations applied to bcc lattice, m_ω are multiplicity factors showing the number of clusters equivalent to ω by symmetry, J_ω are the concentration-independent effective cluster interactions (ECIs), derived from a set of DFT calculations using the structure inversion method, and $\langle \Gamma_\omega, (\vec{\sigma}) \rangle$ are the average correlation functions defined as a product of point functions of occupation variables on a specific cluster ω averaged over all the clusters ω' that are equivalent by symmetry to cluster ω.

The enthalpies of mixing for structures in binary subsystems found in the quaternary Cr-W-Y-Zr system are given in Fig. 3. All bcc structures in binary Cr-W, Cr-Y, Cr-Zr, W-Y and W-Zr systems had positive enthalpy of mixing values, indicating the possibility of atoms segregation in Cr-W-Y-Zr alloys. The highest values (up to 800 meV/atom) were observed for structures in binary Cr-Y and W-Y subsystems.

20 out of 63 binary bcc Y-Zr structures had negative enthalpies of mixing, with the lowest value of − 48 meV/atom observed for Y_5Zr_3 structure, indicating the possibility of atoms ordering between Y and Zr in Cr-W-Y-Zr alloys. The cross-validation error value between the CE and DFT enthalpies of mixing was 18.9 meV/atom.

Values of all the optimized Effective Cluster Interaction (ECIs) for quaternary Cr-W-Y-Zr alloys are shown in Fig. 4 and also in the last column of Table 1. 5 shells for the two-body interactions and two shells for three-body interactions were optimized in these systems. Compared with our previous study for the ternary W-Cr-Y alloys, the 3-body interactions for the third shell have been omitted due to the increase of ECIs for the quaternary alloys. The general expression of the CE Hamiltonian used in the present paper can be written in the form of Eq. (1), where the high-order many-body interactions starting from four-body ones were neglected. It can be seen clearly from Fig. 4 that the two-body ECIs are dominant, whereas the three-body ECIs are relatively

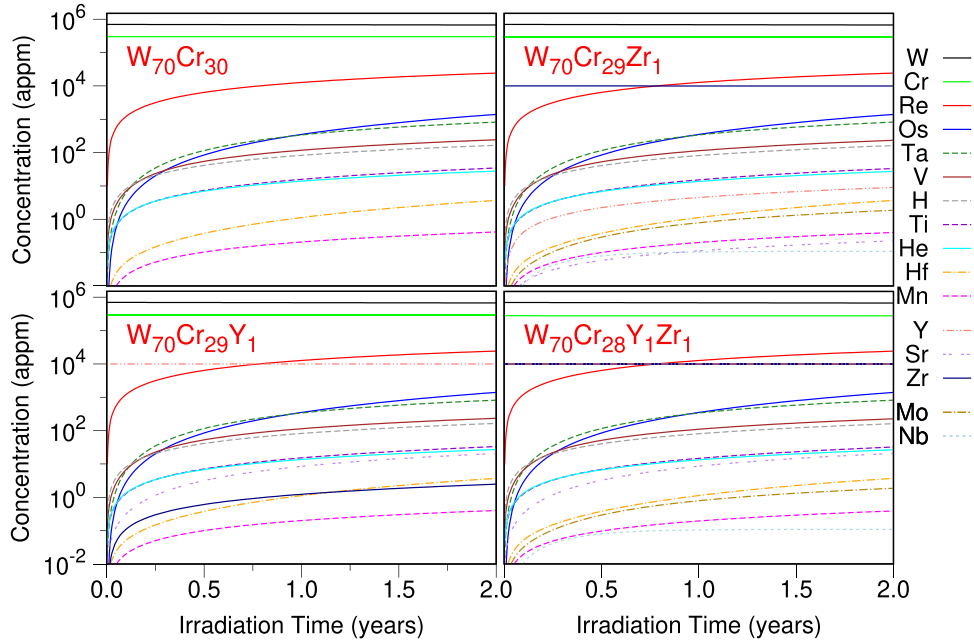

Fig. 1. Transmutation (burn-up) response of $W_{70}Cr_{30}$, $W_{70}Cr_{29}Zr_1$, $W_{70}Cr_{29}Y_1$ and $W_{70}Cr_{28}Y_1Zr_1$ under a typical fusion first wall irradiation exposure.

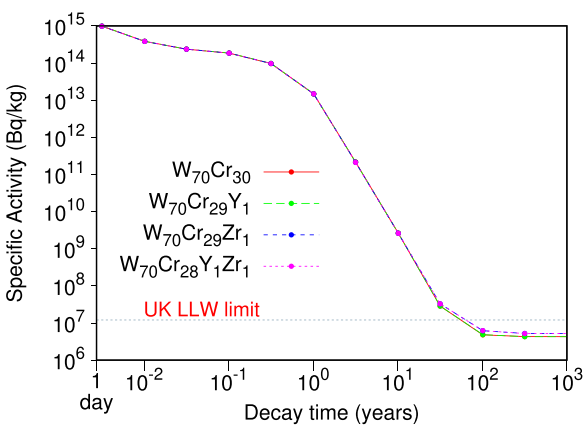

Fig. 2. Radiological response represented by total activity in Bq/kg of $W_{70}Cr_{30}$, $W_{70}Cr_{29}Zr_1$, $W_{70}Cr_{29}Y_1$ and $W_{70}Cr_{28}Y_1Zr_1$ during decay cooling following a two full power year exposure under typical fusion first wall conditions.

small, justifying the convergence of our mapping scheme from DFT to the CE Hamiltonian. It also demonstrates that the understanding of SRO effects in the Cr-W-Y-Zr system can be interpreted from the composition dependence of enthalpies of mixing in the corresponding binary subsystems as shown in Fig. 3.

3.2. Monte Carlo simulations

A $10\times10\times10$ and $30\times30\times30$ bcc unit cells containing 2000 and 54,000 atoms, respectively, were used to perform the Monte Carlo (MC) simulations. Simulations were carried out by quenching down an alloy from a disordered state from high-temperature 3000 K down to 100 K, with a temperature step $\Delta T = 100$ K. 2000 and 1000 MC steps were performed at both accumulation and thermalization stages for the $10\times10\times10$ and $30\times30\times30$ bcc unit cells, respectively. The equilibrium state was been reached at each given temperature, hence the time factor did not play a role in the performed calculations.

The Warren-Cowley Short-Range Order (SRO) parameter was calculated from the pair probabilities y_n^{ij}, obtained for a chosen alloy configuration at considered temperature, following [29,30]:

$$\alpha_n^{ij} = 1 - \frac{y_n^{ij}}{c_i c_j} \tag{2}$$

where i and j are nearest neighbour atoms corresponding to n-th shell while c_i and c_j are concentrations of atoms i and j. The point and pair correlation functions obtained from MC simulations are used to calculate the SRO parameters. Point correlation functions are constant for the specific composition as they are related to the concentrations, whereas pair correlation functions are averaged at the accumulation stage over 2000 MC steps at each temperature. The y_n^{ij} values can be obtained by the inversion of the pair correlation matrix, or by using the analytical formulas [31–33].

For the bcc lattice, the average SRO parameter can be calculated using the first and second nearest neighbours via [34]:

$$\alpha_{avg}^{ij} = \frac{8\alpha_1^{ij} + 6\alpha_2^{ij}}{14} \tag{3}$$

where α_1^{ij} and α_2^{ij} denote the SRO parameters for the 1st and 2nd nearest neighbours, respectively.

The cluster expansion Hamiltonian, defined by Eq. (1), which takes into account all *many*-body cluster interactions, can be used to explicitly determine the configuration entropy of a K-component system via the thermodynamic integration (TDI) method [11]. Here the entropy is computed from fluctuations of the enthalpy of mixing at a given temperature using the following formula:

$$S_{conf}[T] = \int_0^T \frac{C_{conf}(T')}{T'} dT' = \int_0^T \frac{\langle[\Delta H_{mix}^{CE}(T')]^2\rangle - \langle[\Delta H_{mix}^{CE}(T')]\rangle^2}{T'^3} dT' \tag{4}$$

where $\langle[\Delta H_{mix}^{CE}(T')]^2\rangle$ and $\langle[\Delta H_{mix}^{CE}(T')]\rangle^2$ are the square of the mean and mean square enthalpies of mixing, respectively. The average over configurations at finite temperature in Eq. (4) can be performed by combining the CE formalism with MC technique, from which all the simulation steps at the accumulation stage for a given temperature are taken into account. The accuracy of evaluation of configuration entropy from Eq. (4) depends on the size of the temperature integration step and the number of MC steps performed at the accumulation stage.

In this work, semi-canonical exchange MC simulations were also performed using the Alloy Theoretic Automated Toolkit (ATAT) package. For each composition of the K component system, simulations

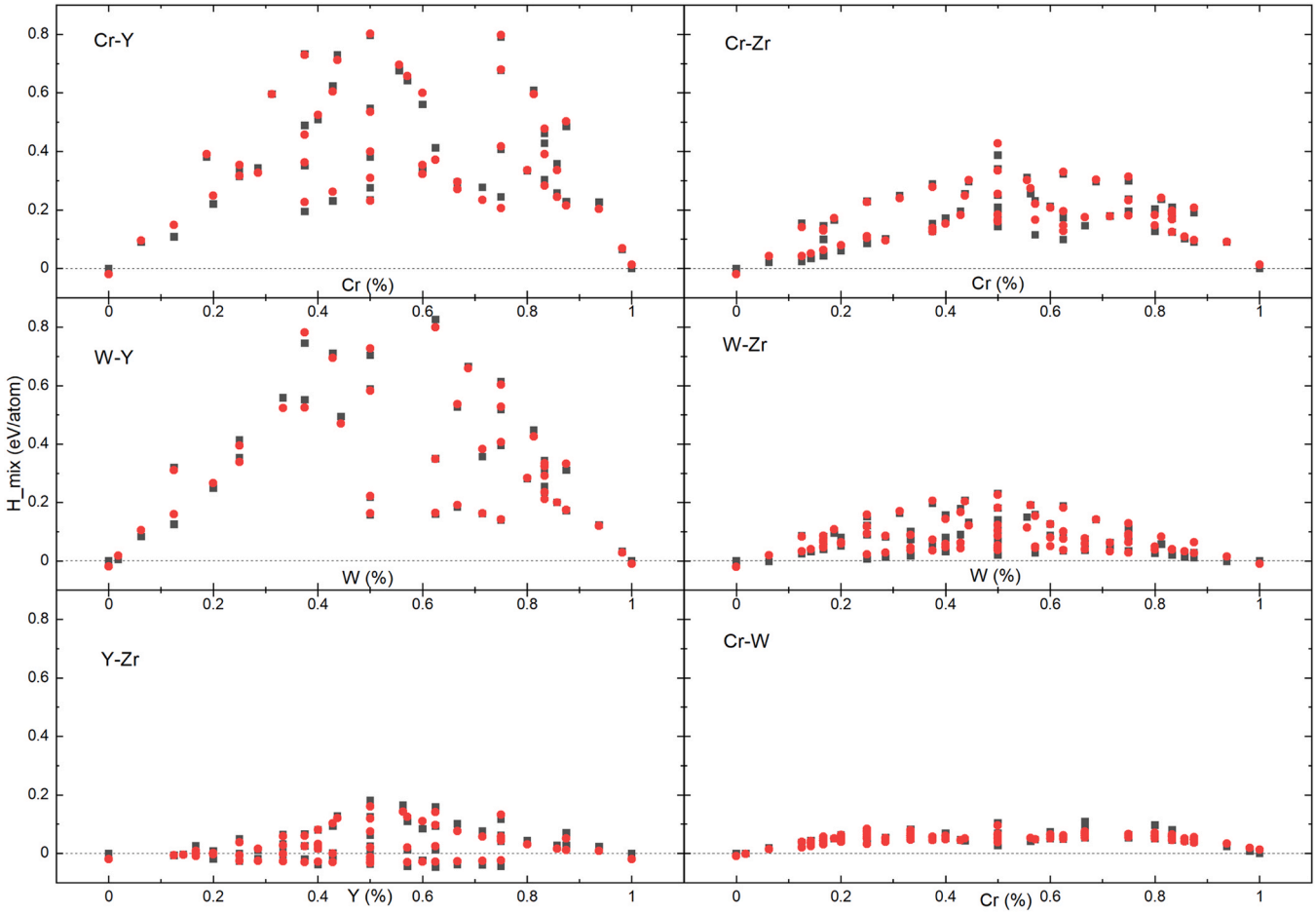

Fig. 3. Enthalpies of mixing of bcc binary structures in Cr-W-Y-Zr system, from DFT (blue) and CE (red) simulations.

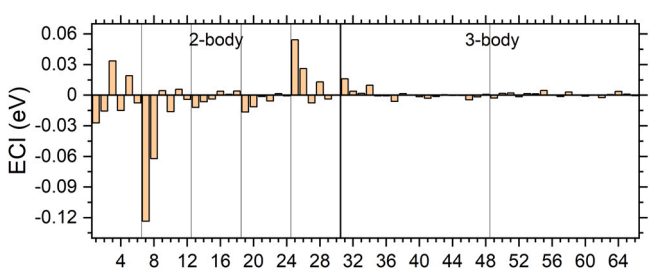

Fig. 4. Effective cluster interactions for quaternary Cr-W-Y-Zr system.

were performed starting from a disordered, high-temperature state at $T = 3000$ K. The system was then quenched down with a temperature step of $\Delta T = 10$ K, with 2000 equilibration and accumulation MC steps at a given temperature within the TDI method. With the definition of configuration entropy from Eq. (4), the hybrid CE-MC method enables the evaluation of the configuration free energy:

$$F_{conf}(T) = E_{mix}(T) - TS_{conf}(T) \tag{5}$$

We can also define the excess configuration entropy of mixing as a difference between the random configuration entropy at a high-temperature limit and those of configuration at a finite temperature as follows:

$$S_{mix} = S_{rand} - S_{conf} \tag{6}$$

where S_{rand} is the entropy of a random configuration using the formula:

$$S_{rand} = -k_B \sum_i c_i ln(c_i) \tag{7}$$

Finally, the free energy of mixing can be obtained from the excess configuration entropy of mixing as it has been defined in [12];

$$F_{mix}(T) = H_{mix}(T) - TS_{mix}(T) \tag{8}$$

4. Finite temperature phase stability and short-range ordering

MC simulations for ternary $W_{70}Cr_{29}Zr_1$ as well as quaternary $W_{70}Cr_{28}Y_1Zr_1$ and $W_{70}Cr_{29}Y_{0.5}Zr_{0.5}$ alloys were carried out by using the ATAT package. To calculate the enthalpy of mixing and short-range ordering (SRO), the simulations were performed on the $10 \times 10 \times 10$ bcc unit cells containing 2000 atoms by quenching down from 3000 K to 100 K with a 100 K temperature step. Additionally, MC simulations were also performed on the $30 \times 30 \times 30$ bcc unit cells by quenching down from 2000 K to visualize better the structures obtained at finite temperatures.

4.1. SRO in ternary W-Cr-Zr system and the comparison with W-Cr-Y alloys

In Fig. 5a, the SRO parameter values are given for pairs in the ternary $W_{70}Cr_{29}Zr_1$ alloy, compared to the $W_{70}Cr_{29}Y_1$ alloy (Fig. 5b). The Cr-W and Cr-Zr pairs had positive values of the enthalpy of mixing in the whole temperature range. The W-Zr pair had a negative value of the enthalpy of mixing between 500 K and 3000 K, while having positive values below 500 K.

The behavior of the W-Zr pair can be used to describe the formation of the Zr cluster, observed in Fig. 6a in the analyzed alloy. Starting from 3000 K, while quenching down the alloy, the Zr atoms are mostly neutral when it comes to their behavior towards W and Cr atoms.

Table 1
Effective cluster interactions obtained for the Cr-W-Y-Zr system. Cluster size is denoted by $|\omega|$, shell label is denoted by n, $m^{(s)}_{|\omega|,n}$ denotes multiplicities and $J^{(s)}_{|\omega|,n}$ are the concentration-independent effective cluster interactions in eV.

$\|\omega\|$	n	$m^{(s)}_{\|\omega\|,n}$	$J^{(s)}_{\|\omega\|,n}$	$\|\omega\|$	n	$m^{(s)}_{\|\omega\|,n}$	$J^{(s)}_{\|\omega\|,n}$
1	1	1	0.384636	3	1	12	0.015986
		1	0.032608			24	0.003846
		1	− 0.183974			24	0.001887
		1	− 0.253236			12	0.009868
2	1	4	− 0.027111			24	− 0.000654
		8	− 0.015458			24	− 0.000623
		8	0.033531			12	− 0.005993
		4	− 0.015028			24	0.001551
		8	0.019156			24	− 0.000155
		4	− 0.007447			12	− 0.00135
2	2	3	− 0.123479			24	− 0.002951
		6	− 0.062111			12	− 0.001266
		6	0.004498			24	0.000495
		3	− 0.016112			12	− 0.000255
		6	0.005754			24	− 0.000365
		3	− 0.004108			12	− 0.004569
2	3	6	− 0.011881			12	− 0.001679
		12	− 0.006327			12	0.000867
		12	− 0.003643	3	2	12	− 0.002715
		6	0.003901			24	0.001704
		12	0.000922			24	0.002166
		6	0.004018			12	− 0.001529
2	4	12	− 0.016445			24	0.001665
		24	− 0.011315			24	0.001445
		24	− 0.001233			12	0.004708
		12	− 0.005632			24	− 0.000006
		24	0.001509			24	− 0.001336
		12	− 0.000647			12	0.003081
2	5	4	0.054353			24	− 0.000124
		8	0.026202			12	− 0.000962
		8	− 0.007527			24	− 0.000198
		4	0.013056			12	− 0.00239
		8	− 0.003772			24	0.00067
		4	0.000068			12	0.003694
						12	0.001126
						12	− 0.000523

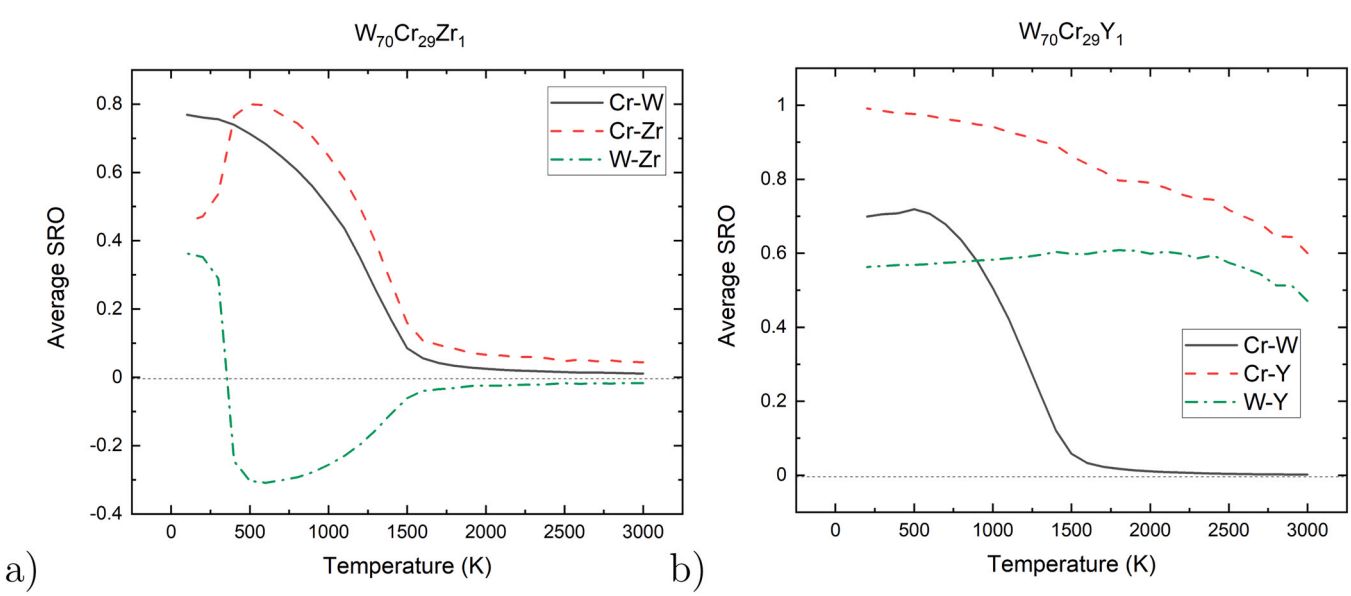

Fig. 5. Average short-range order parameters in a) $W_{70}Cr_{29}Zr_1$ and b) $W_{70}Cr_{29}Y_1$ alloys.

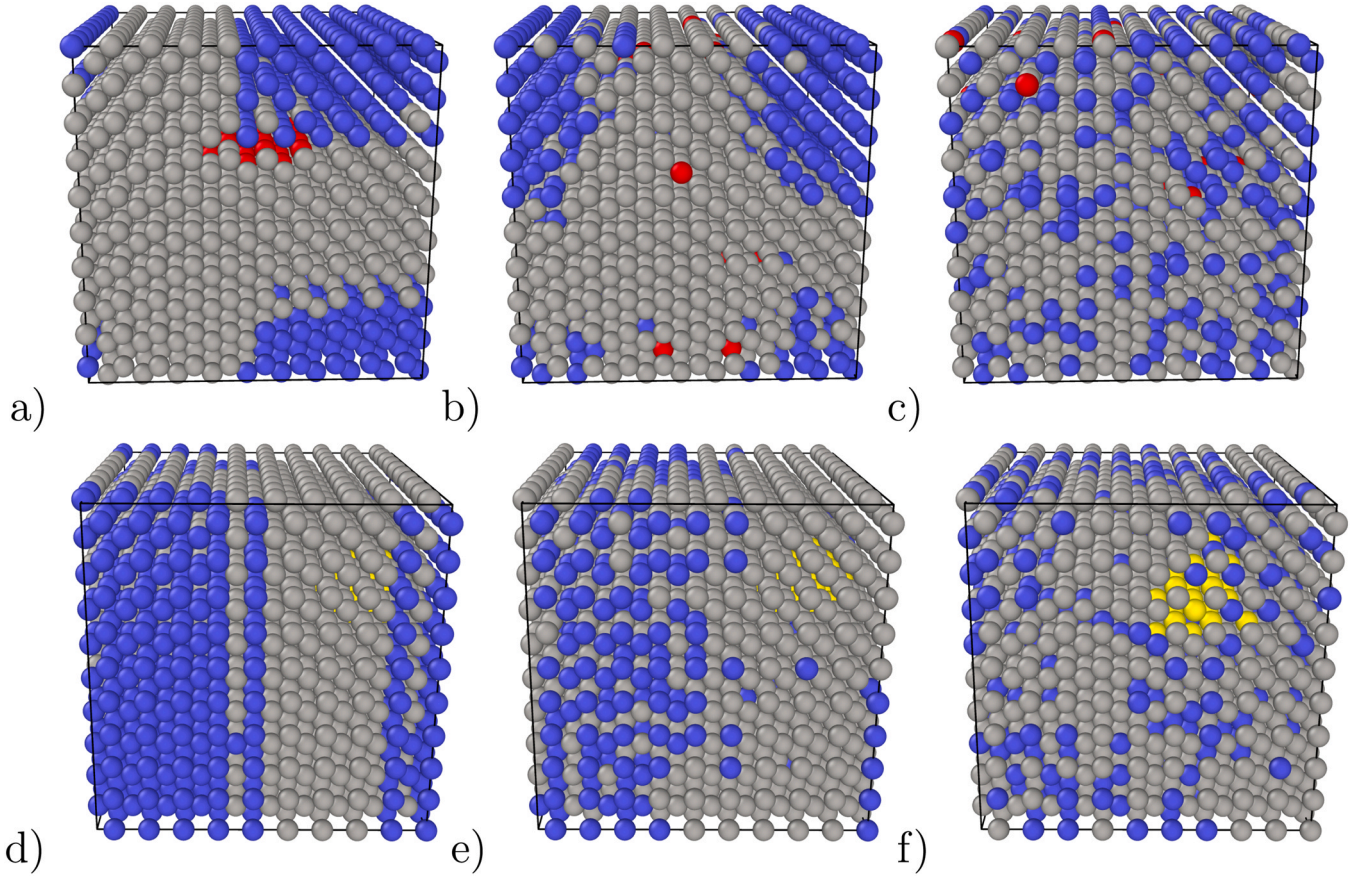

Fig. 6. Structure images for $W_{70}Cr_{29}Zr_1$ alloy at a) 300 K, b) 800 K and c) 1800 K in comparison with $W_{70}Cr_{29}Y_1$ alloy at d) 300 K, e) 800 K and f) 1800 K.

Starting from around 1600 K, the Zr atoms start to separate from Cr atoms and are found mostly in the neighbourhood of W atoms (Fig. 6c). At around 600 K, the Zr-rich cluster is being formed, which is observed as a shift of the W-Zr SRO parameter from negative to positive, as Zr atoms are now mostly found within the Zr-rich cluster. At low temperatures, we are therefore observing a strong separation into the Cr layer, W layer, and the Zr precipitation.

4.2. SRO in quaternary W-Cr-Y-Zr as a function of alloy composition and temperature

In Fig. 7a the SRO parameter values are given for pairs in the quaternary $W_{70}Cr_{28}Y_1Zr_1$ alloy. Negative values in the whole temperature range were observed for the Y-Zr pair indicating the attraction between Y and Zr atoms and the possibility of clustering in the alloy. The highest positive values of the SRO parameter in the whole temperature range were observed for the Cr-Y pair. The remaining pairs of atoms (Cr-W, Cr-Zr, W-Y and W-Zr) also had positive values of the SRO parameter indicating repulsion and a strong tendency towards segregation in the alloy.

In Fig. 7b, the SRO parameter values are given for pairs in the quaternary $W_{70}Cr_{29}Y_{0.5}Zr_{0.5}$ alloy. Similarly to the $W_{70}Cr_{28}Y_1Zr_1$ alloy, the Y-Zr has negative and Cr-Y the most positive values in the whole temperature range, with the remaining pairs SRO values being positive. Compared to the $W_{70}Cr_{28}Y_1Zr_1$ alloy, the SRO parameter values of pairs found in the $W_{70}Cr_{29}Y_{0.5}Zr_{0.5}$ are starting to shift towards 0 above 2500 K.

A comparison of the SRO between Cr and W, which characterizes spinodal phase decomposition in SMART materials, is shown in Fig. 8. It is found from our systematic study that the average SRO parameter value for the Cr-W pair increases from ternary systems: $W_{70}Cr_{29}Y_1$ and $W_{70}Cr_{29}Zr_1$ to the quaternary $W_{70}Cr_{28}Y_1Zr_1$ and $W_{70}Cr_{29}Y_{0.5}Zr_{0.5}$ alloys before reaching to the maximum value in the binary $W_{70}Cr_{30}$.

In Fig. 9, the $30 \times 30 \times 30$ unit cells structure images are given for the $W_{70}Cr_{28}Y_1Zr_1$ alloy at 300 K, 1000 K, and 1800 K temperatures, containing 54000 atoms. In Fig. 9a there was observed a big cylindrical-shape precipitation of Cr (blue atoms) inside the W (grey atoms), which was still present but started to disintegrate at 1000 K (Fig. 9b), while being completely vanished at 1800 K (Fig. 9c), which is in agreement with the Cr-W pair SRO parameter values presented in Fig. 7a (SRO parameter values being close to 0 above 1500 K). At all temperatures, the Y-Zr spherical precipitation was also observed, with the Y (yellow) atoms occupying the inside of the precipitation and Zr (red) atoms surrounding it, separating the Y atoms from W. The formation of Y-Zr precipitation was expected from the initial DFT and CE calculations, which indicated that for the Cr-Y-W-Zr alloy, only that pair had the negative values of the enthalpy of mixing, and it was also the only pair with the negative SRO parameter values.

In Fig. 10, the $30 \times 30 \times 30$ unit cells structure images are given for the $W_{70}Cr_{29}Y_{0.5}Zr_{0.5}$ alloy at 400 K, 1000 K and 1800 K temperatures, containing 54,000 atoms. In Fig. 10a, there was observed big spherical precipitation of Cr, which was still present but started to disintegrate at 1000 K (Fig. 10b) while completely vanished at 1800 K (Fig. 10c),

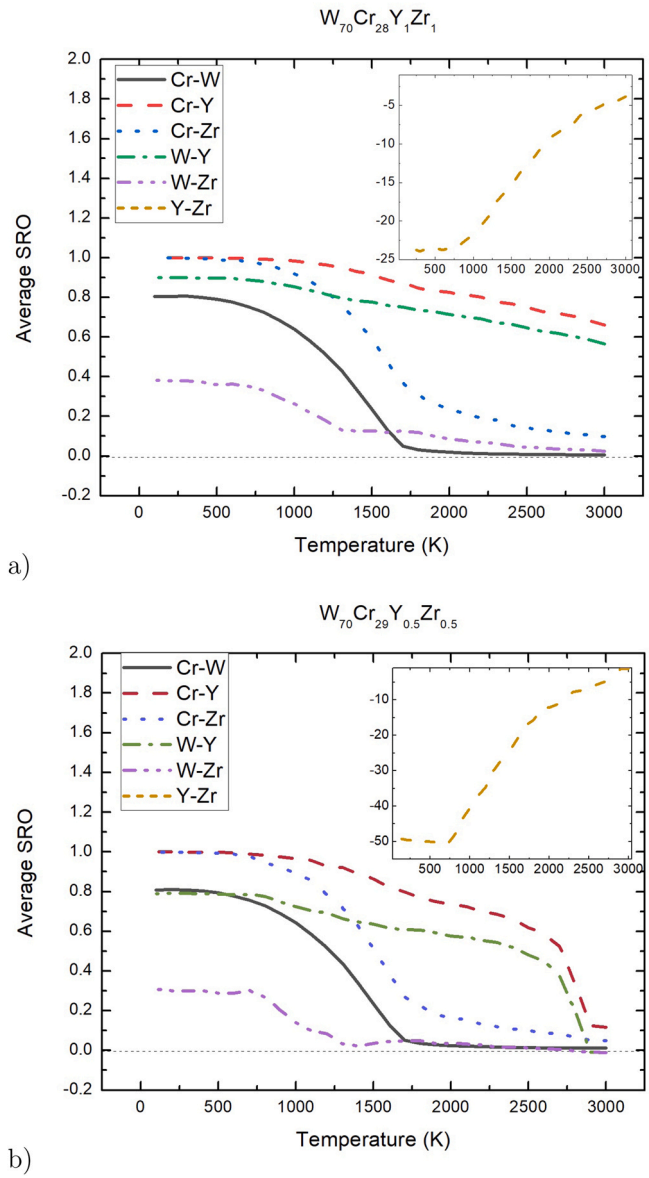

Fig. 7. Average short-range order parameters in a) $W_{70}Cr_{28}Y_1Zr_1$ and b) $W_{70}Cr_{29}Y_{0.5}Zr_{0.5}$ alloys. Insets visualize a wider range of scales to clearly reflect the Y-Zr pair SRO parameter values.

which is also in agreement with the Cr-W pair SRO parameter values presented in Fig. 7b. Similarly to $W_{70}Cr_{28}Y_1Zr_1$, the Y-Zr spherical precipitation was also observed at all temperatures, with the Y atoms occupying the inside of the precipitation and Zr atoms surrounding it.

4.3. Free energy calculations

In Fig. 11 the enthalpy of mixing as a function of temperature for $W_{70}Cr_{28}Y_1Zr_1$ and $W_{70}Cr_{29}Y_{0.5}Zr_{0.5}$ alloys in comparison with the $W_{70}Cr_{30}$ alloy is given. In the whole temperature range, the values of enthalpy of mixing were positive for all three analyzed compositions. The addition of Y and Zr decreased the enthalpy of mixing value by about 15 meV/atom at lower temperatures (below 1000 K), with the difference diminishing with the increase of the temperature. Between 1500 K and 2500 K, the $W_{70}Cr_{29}Y_{0.5}Zr_{0.5}$ alloy had lower enthalpy of mixing than $W_{70}Cr_{28}Y_1Zr_1$ by around 5 meV/atom.

Fig. 12 compare the calculated random entropy (Eq. (7)), the configurational entropy (Eq. (4)), and the excess configuration entropy of

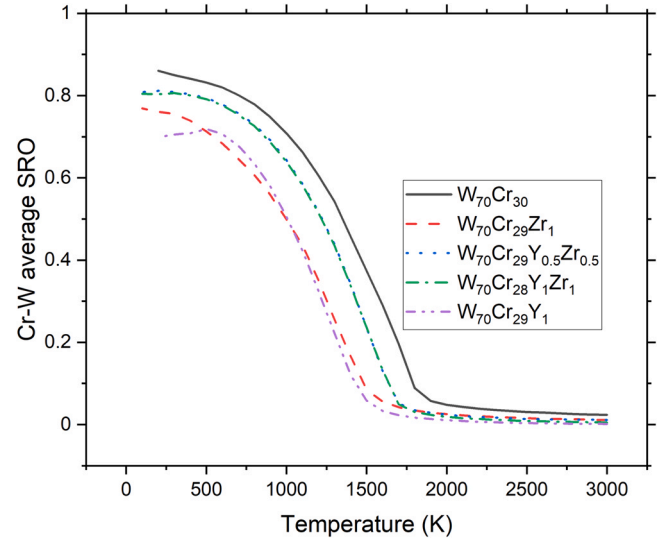

Fig. 8. Average short-range order parameter values for Cr-W in $W_{70}Cr_{29}Zr_1$, $W_{70}Cr_{29}Y_1$, $W_{70}Cr_{29}Y_{0.5}Zr_{0.5}$ and $W_{70}Cr_{28}Y_1Zr_1$ alloys in comparison with $W_{70}Cr_{30}$ alloy.

mixing (Eq. (6)) for the $W_{70}Cr_{29}Zr_1$, $W_{70}Cr_{28}Y_1Zr_1$ and $W_{70}Cr_{29}Y_{0.5}Zr_{0.5}$ alloys in comparison with the $W_{70}Cr_{29}Y_1$ alloys. The linear temperature dependence of the random configuration entropy (Fig. 12a) represents the maximum theoretical value of the entropy contribution for a given composition and is highest in the whole temperature range for the $W_{70}Cr_{28}Y_1Zr_1$ alloy (hence the lowest value of the $-TS_{rand}$ expression). The configurational entropy shown in Fig. 12b has been calculated by the TDI. Finally, Fig. 12c shows the difference between configuration entropy from random and the corresponding ones obtained by the TDI method. The highest entropy of mixing contribution is observed for the $W_{70}Cr_{28}Y_1Zr_1$ alloy in the whole temperature range (which is observed as the lowest value of the $(-T(S_{rand}-S_{conf}))$ expression.

The configuration free energy calculated from Eq. (5) and the free energy of mixing obtained from Eq. (8) shown in Fig. 13a and b, respectively, are given for the $W_{70}Cr_{29}Zr_1$, $W_{70}Cr_{28}Y_1Zr_1$ and $W_{70}Cr_{29}Y_{0.5}Zr_{0.5}$ alloys in comparison with the $W_{70}Cr_{29}Y_1$ alloy. Below 1500 K, the highest values of the free energy of mixing are observed for the $W_{70}Cr_{29}Y_1$ alloy, up to over 60 meV/atom at 1500 K. The lowest values of the free energy of mixing in the whole temperature range were observed for the $W_{70}Cr_{28}Y_1Zr_1$ alloy, with slightly higher values for the $W_{70}Cr_{29}Y_{0.5}Zr_{0.5}$ alloy. It is worth noting that both the $W_{70}Cr_{28}Y_1Zr_1$ and the $W_{70}Cr_{29}Y_{0.5}Zr_{0.5}$ alloys showed negative values of the free energy of mixing between 300 K and around 1100–1200 K. Both $W_{70}Cr_{29}Y_1$ and $W_{70}Cr_{29}Zr_1$ showed positive values of the free energy of mixing in the whole temperature range.

5. Discussion

5.1. Application of the model to a wider range of compositions

The developed model for the W-Cr-Y-Zr system allows investigation of the phase stability and short-range ordering of alloys with arbitrary composition and temperature range. For example, simulations extending to the equiatomic quaternary W-Cr-Y-Zr alloy were carried out to more thoroughly investigate the behavior of W, Cr and Y in the presence of Zr in an alloy. In Fig. 14, the short-range order parameter as a function of temperature value is given for pairs of atoms present in the specified alloy. At around 1100 K and above, a shift from positive to negative SRO parameter value is observed for Y-Zr and Cr-W pairs. With all remaining pairs SRO values being positive in the whole temperature range, this indicates that at higher temperatures, we should observe a phase

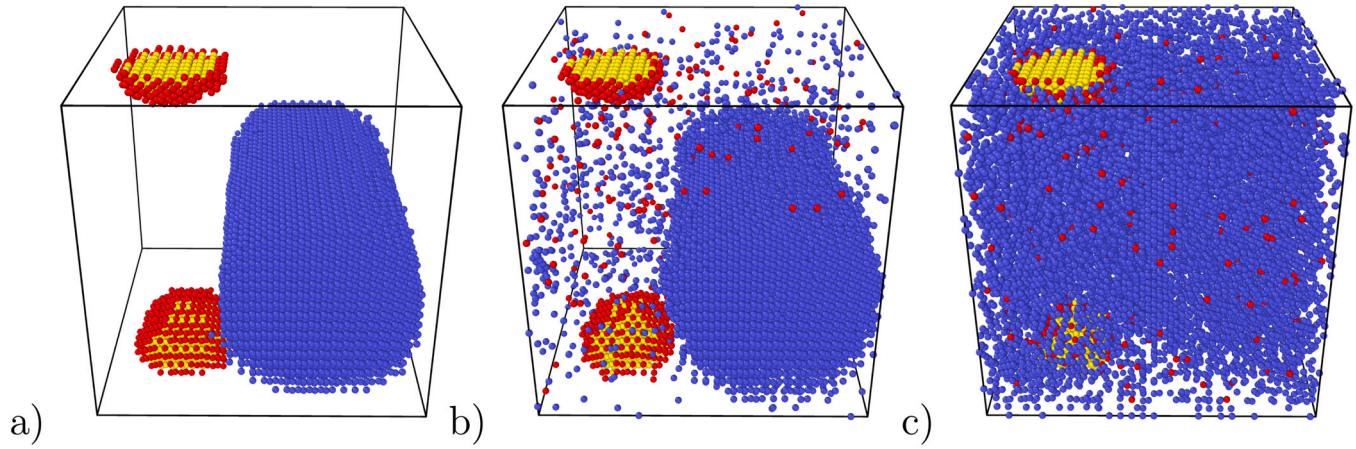

Fig. 9. Structure images for $W_{70}Cr_{28}Y_1Zr_1$ alloy at a) 300 K, b) 1000 K and c) 1800 K. W atoms were removed from the image for better visualization of the cluster of Cr (blue), Y (yellow) and Zr (red) atoms.

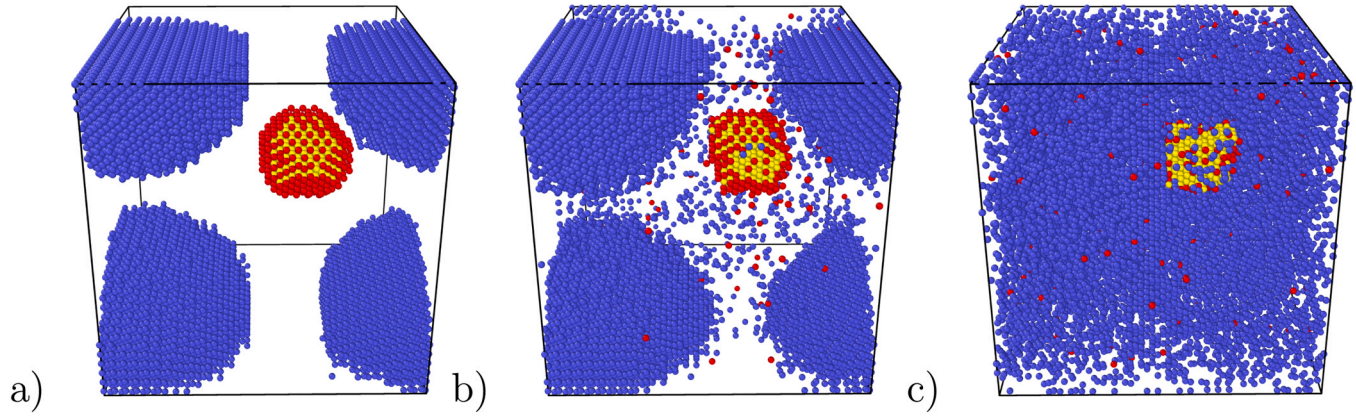

Fig. 10. Structure images for $W_{70}Cr_{29}Y_{0.5}Zr_{0.5}$ alloy at a) 400 K, b) 1000 K and c) 1800 K. W atoms were removed from the image for better visualization of the cluster of Cr (blue), Y (yellow) and Zr (red) atoms.

separation between Y/Zr and Cr/W phases. In contrast, at temperatures below 1100 K, there is a tendency toward segregating each element in the alloy. These predictions were confirmed by visualizing structures obtained at 300 K, 1200 K, and 1800 K and presented in Fig. 15. At 300 K (Fig. 15a), a layer-like structure is observed with alternating layers of Y and Zr in the middle of the simulation cell, through W and Cr layers to the outer of the cell. With the increase of the temperature (Fig. 15b,c), the Y and Zr atoms mix with each other while still being separated from the W and Cr, which also start to mix into the W/Cr-rich phase.

5.2. Experimental validation of modeling results

Results shown in the present study provide a further, more detailed look into the Y and Zr behavior in ternary $W_{70}Cr_{29}Zr_1$ as well as quaternary $W_{70}Cr_{28}Y_1Zr_1$ and $W_{70}Cr_{29}Y_{0.5}Zr_{0.5}$ alloys, which have already been experimentally validated as promising candidates for future fusion applications [8,9].

Available study shows that an extremely fine nanoparticle dispersion is observed in as-HIPed W-10Cr-0.5Y-0.5Zr (wt%, which is equivalent to around $W_{70}Cr_{28}Y_1Zr_1$ at%) alloy, and even though average grain size grows from below 100–620 nm after heat treatment at 1555°C for 1.5 h, the nanoparticles are still present at both the grain

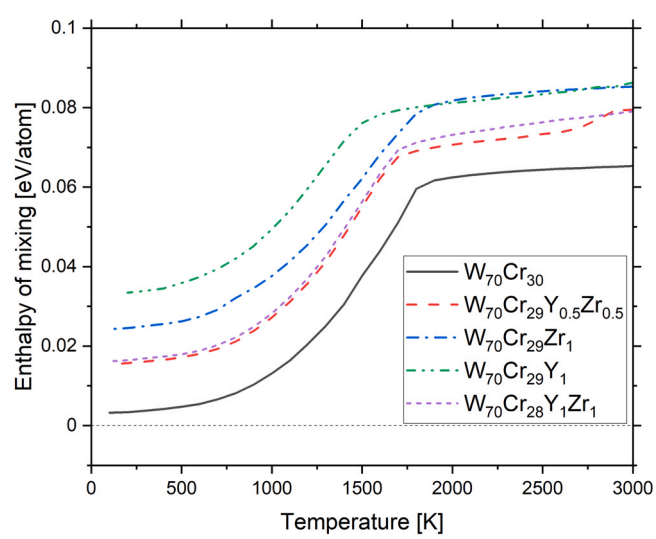

Fig. 11. Enthalpy of mixing as a function of temperature of the $W_{70}Cr_{29}Zr_1$, $W_{70}Cr_{28}Y_1Zr_1$ and $W_{70}Cr_{29}Y_{0.5}Zr_{0.5}$ alloys in comparison with the $W_{70}Cr_{30}$, $W_{70}Cr_{29}Y_1$ and $W_{70}Cr_{29}Zr_1$ alloys.

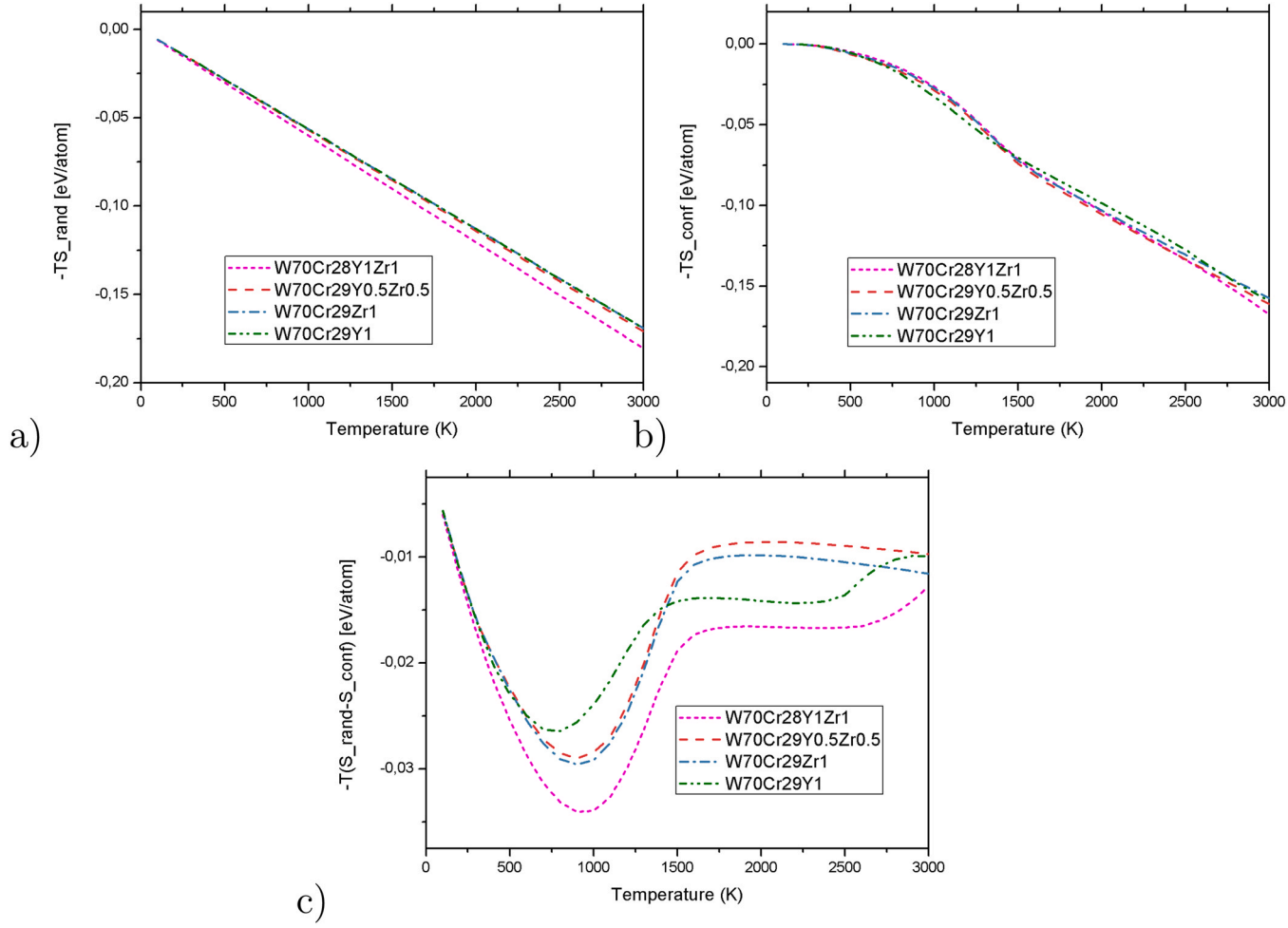

Fig. 12. The random configuration entropy (a), the TDI configurational entropy (b) and the entropy of mixing (c) for $W_{70}Cr_{29}Zr_1$, $W_{70}Cr_{28}Y_1Zr_1$ and $W_{70}Cr_{29}Y_{0.5}Zr_{0.5}$ alloys in comparison with the $W_{70}Cr_{29}Y_1$ alloy.

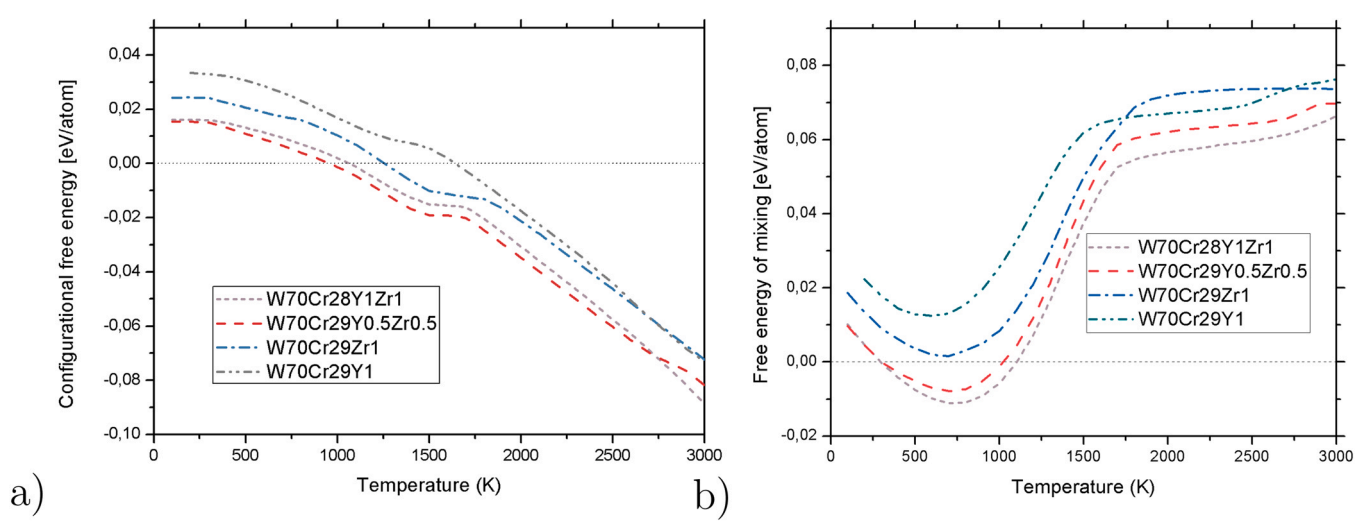

Fig. 13. Configuration free energy from the TDI (a) and free energy of mixing (b) calculated for $W_{70}Cr_{29}Zr_1$, $W_{70}Cr_{28}Y_1Zr_1$ and $W_{70}Cr_{29}Y_{0.5}Zr_{0.5}$ alloys in comparison with the $W_{70}Cr_{29}Y_1$ alloy.

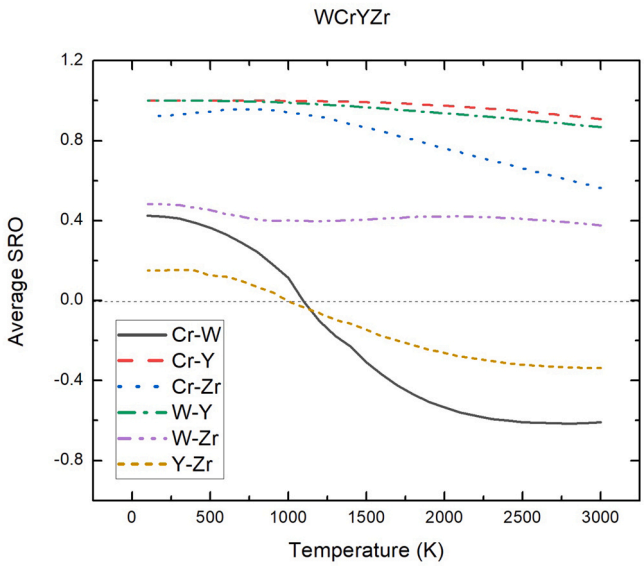

Fig. 14. Average short-range order parameter values for equiatomic W-Cr-Y-Zr alloy as a function of temperature.

boundaries and inside the grains [9]. The presence of those particles can be explained by our MC results, which show that both Y and Zr strongly segregate from an alloy, separating themselves and forming Y/Zr rich clusters even at elevated temperatures (Fig. 9c).

The same study has also provided a look into the microstructure of a ternary W-10Cr-0.5Zr (wt%, which is equivalent to around $W_{71}Cr_{28}Zr_1$ at%) alloy, both as-HIPed and after the heat treatment at 1555°C for 1.5 h [9]. The observed Zr-containing nanoparticles were significantly larger in size than those containing both Y and Zr in quaternary alloys while being mostly found inside the matrix grains instead of at grain boundaries. Those results are in general agreement with our MC results, which showed that in ternary $W_{70}Cr_{29}Zr_1$ alloy, the Zr-rich clusters are being formed below 500 K, a much lower temperature than that of Y/Zr-rich clusters formation observed in quaternary W-Cr-Y-Zr alloys.

Another experimental study looked into the microstructure evolution of the ternary W-11.4Cr-1.0Zr (wt%) alloy consolidated by the field-assisted sintering technology (FAST) [8]. In the referenced study, the cross-section SEM analysis of the samples revealed the presence of Cr-rich phases as well as Zr-rich nanoparticles. Those results are in general agreement with our MC results, which showed the presence of Zr-rich cluster at temperatures below 500 K, as well as the separation of Cr from W even at around 800 K (Fig. 6a,b,c). The same study has also concluded that with the increase of sintering temperature up to 1250°C, the content of the Cr-rich phase in W-11.4Cr-1.0Zr (wt%) alloy declines steeply. This is in agreement with our MC results, specifically with the SRO parameter value predicted for the Cr-W pair in the ternary $W_{70}Cr_{29}Zr_1$ alloy (Fig. 5a), which is strongly negative at lower temperatures while quickly coming closer to 0 above 1500 K.

6. Conclusions

A DFT-based Cluster Expansion (CE) model has been developed for the quaternary bcc Cr-W-Y-Zr system. All binary structures found in Cr-W, Cr-Y, Cr-Zr, W-Y, and W-Zr systems showed positive values of the enthalpy of mixing. The only structures with negative values of the enthalpy of mixing were found in the Y-Zr binary system.

The CE Hamiltonian has been developed to be used in the MC simulations in order to investigate the phase stability and short-range ordering of the ternary $W_{70}Cr_{29}Zr_1$ as well as quaternary $W_{70}Cr_{28}Y_1Zr_1$ and $W_{70}Cr_{29}Y_{0.5}Zr_{0.5}$ alloys.

Formation of the Zr-rich cluster has been observed at temperatures around 500 K and below in ternary $W_{70}Cr_{29}Zr_1$ alloy. The clustering is a result of the short-range ordering change between W-Zr – from segregation above 500 K (positive values of the SRO parameter) to ordering below 500 K (negative values of the SRO parameter). While trying to separate itself from W, the Zr starts forming a Zr-rich cluster since its SRO parameter with Cr is also positive below 500 K.

In quaternary $W_{70}Cr_{28}Y_1Zr_1$ and $W_{70}Cr_{29}Y_{0.5}Zr_{0.5}$ alloys, the formation of Y-Zr cluster has been observed at elevated temperatures up to 1800 K. The Y-Zr pair had a negative value of the SRO parameter in the whole temperature range, while all remaining pairs showed positive values.

The enthalpy of mixing of the $W_{70}Cr_{29}Zr_1$ alloy was higher than the enthalpy of mixing of the $W_{70}Cr_{30}$ alloy in the whole temperature range by around 20 meV/atom while being lower than the enthalpy of mixing of the $W_{70}Cr_{29}Y_1$ alloy below 1800 K by around 10 meV/atom. The co-existence of the Y and Zr in the analyzed alloy resulted in lower enthalpy of mixing value than those for ternary $W_{70}Cr_{29}Zr_1$ and $W_{70}Cr_{29}Y_1$ alloys, but higher than that for the $W_{70}Cr_{30}$ alloy in the whole temperature range.

The average SRO parameter value for the Cr-W pair in the quaternary $W_{70}Cr_{28}Y_1Zr_1$ and $W_{70}Cr_{29}Y_{0.5}Zr_{0.5}$ alloys was found to be between the SRO parameter values for the binary $W_{70}Cr_{30}$, and ternary $W_{70}Cr_{29}Zr_1$ and $W_{70}Cr_{29}Y_1$ alloys. It is worth emphasizing here again that the predicted positive short-range order for the Cr-W pairs indicates a strong presence of spinodal phase segregation between W and Cr in the quaternary W-Cr-Y-Zr system. Finally, the present modeling

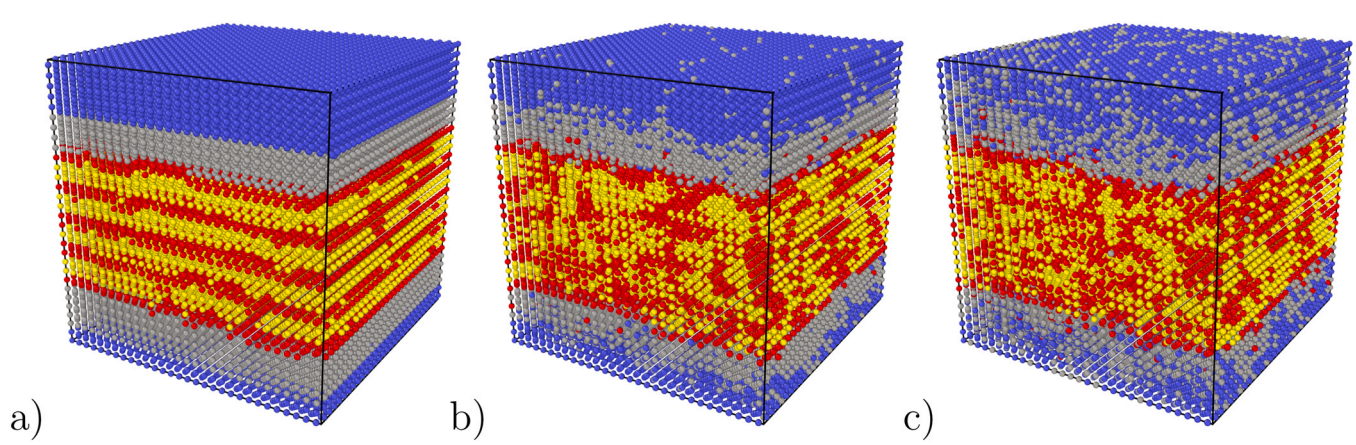

Fig. 15. Structure images for equiatomic WCrYZr alloy at a) 300 K, b) 1200 K, and c) 1800 K. Atoms are represented by colors: W (grey), Cr (blue), Y (yellow), and Zr (red).

work demonstrates strong segregation of both Y and Zr due to negative SRO between them and other atoms in self-passivating W-Cr-Y-Zr alloys at high temperatures supporting the existence of small nano-particles observed in the microstructure of self passivating W-Cr-Y-Zr alloys after heat treatment at high temperature [9].

In conclusion, the presented work provides understanding of the underlying phenomena of microstructure evolution in the recently experimentally studied W-Cr-Y-Zr SMART materials [8,9]. Compared with the ternary W-Cr-Y, the Y-Zr negative short-range ordering enhances the positive short-range ordering between Cr and W in the quaternary W-Cr-Y-Zr. Our modeling results confirm that the spinodal microstructure plays an important role in increasing the mechanical strength of the ternary $W_{70}Cr_{29}Y_1$ alloy after neutron irradiation, which has been observed recently in [7]. Therefore the significant impact of the spinodal phase segregation between Cr and W has been revealed, which is crucial to the suitability of the anticipated use of SMART materials as fusion first wall components.

Declaration of Competing Interest

The authors declare that they have no known competing financial interests or personal relationships that could have appeared to influence the work reported in this paper.

Acknowledgements

This work has been carried out within the framework of the EUROfusion Consortium, funded by the European Union via the Euratom Research and Training Programme (Grant Agreement No 101052200 -Ť EUROfusion) and was partially supported by the Broader Approach Phase II agreement under the PA of IFERC2-T2PA02. Views and opinions expressed are however those of the author(s) only and do not necessarily reflect those of the European Union or the European Commission. Neither the European Union nor the European Commission can be held responsible for them.

MRG and DNM acknowledge funding from the RCUK Energy Programme Grant No. EP/W006839/1. The work at WUT has been carried out as a part of an international project co-financed by the Polish Minister of Science and Higher Education through the PMW program in 2022; Agreement No. 5257/HEU-EURATOM/2022/2. JSW, DS and DNM would like to acknowledge the use of the high-performance computing facility MARCONI (Bologna, Italy) provided by EUROfusion. The authors would like to thank Prof. Andrey Litnovsky for his valuable comments on this work.

References

[1] G. Pintsuk, et al., Materials for in-vessel components, Fusion Eng. Des. 174 (2022) 112994, , https://doi.org/10.10161/j.fusengdes.2021.112944
[2] E. Lassner, W.D. Schubert, Tungsten – properties, chemistry, technology of the elements, Alloys and Chemical Compounds, Kluwer, Dordrecht, 1999.
[3] M. Gilbert, et al., Activation, decay heat, and waste classification studies of the European DEMO concept, Nucl. Fusion 57 (2017) 046015, , https://doi.org/10.1088/1741-4326/aa5bd7
[4] A. Litnovsky, et al., Smart tungsten-based alloys for a first wakk of DEMO, Fusion Eng. Des. 159 (2020) 111742, , https://doi.org/10.10161/j.fusengdes.2020.111742
[5] F. Koch, H. Bolt, Self-passivating W-based alloys as plasma facing material for nuclear fusion, Phys. Scr. 128 (2007) 100–105, https://doi.org/10.1088/0031-8949/2007/T128/020
[6] F. Koch, et al., Oxidation behaviour of silicon-free tungsten alloys for use as the first wall material, Phys. Scr. 145 (2011) 014019, , https://doi.org/10.1088/0031-8949/2011/T145/014019
[7] D. Terentyev, et al., Development of irradiation tolerant tungsten alloys for high temperature nuclear application, Nucl. Fusion 62 (2022) 086035, , https://doi.org/10.1088/1741-4326/ac75fe
[8] W.J. Wang, et al., The influence of powder characteristics on densification behaviour and microstructure evolution of W-Cr-Zr alloy consolidated by field-assisted sintering technology, Int. J. Refract. Met. Hard Mater. 108 (2022) 105939, , https://doi.org/10.1016/j.ijrmhm.2022.105939
[9] E. Sal, et al., Microstructure, oxidation behaviour and thermal shock resistance of self-passivating W-Cr-Y-Zr alloys, Nucl. Mater. Energy 24 (2020) 100770, , https://doi.org/10.1016/j.nme.2020.100770
[10] O. El-Atwani, et al., Outstanding radiation resistance of tungsten-based high-entropy alloys, Sci. Adv. 5 (2021) eaav2022.
[11] D. Nguyen-Manh, et al., First-principles modelling for voids decorated by transmutation solutes: Short-range order effects and application to neutron irradiated tungsten, Phys. Rev. Mater. 5 (2021) 065401, , https://doi.org/10.1103/PhysRevMaterials.5.065401
[12] D. Sobieraj, et al., Chemical short-range order in derivative Cr-Ta-Ti-V-W high-entropy alloys from the first-principles thermodynamic study, Phys. Chem. Chem. Phys. 22 (2020) 23929, https://doi.org/10.1039/d0cp03764h
[13] D. Sobieraj, et al., Composition stability and Cr-rich phase formation in W-Cr-Y and W-Cr-Ti smart alloys, Metals 11 (2021) 743, https://doi.org/10.3390/met11050743
[14] A. Litnovsky, et al., Advanced self-passivating alloys for an application under extreme conditions, Metals 11 (2021) 1125, https://doi.org/10.3390/met1081255
[15] U. Fischer, C. Bachmann, J.P. Catalan, T. Eade, D. Flammini, M.R. Gilbert, J.-Ch. Jaboulay, A. Konobeev, D. Leichtle, L. Lu, F. Malouch, F. Moro, P. Pereslavtsev, Y. Qiu, L. Sanz, P. Sauvan, G. Stankunas, A. Travleev, A. Turner, F. Ogando, I. Palermo, R. Villari, Methodological approach for DEMO neutronics in the European PPPT programme: Tools, data and analyses, Fusion Eng. Des. 123 (2017) 26–31, https://doi.org/10.1016/j.fusengdes.2017.01.053
[16] G. Federici, W. Biel, M.R. Gilbert, R. Kemp, N. Taylor, R. Wenninger, European DEMO design strategy and consequences for materials, Nucl. Fusion 57 (2017) 092002, , https://doi.org/10.1088/1741-4326/57/9/092002
[17] G. Federici, C. Bachmann, L. Barucca, W. Biel, L. Boccaccini, R. Brown, C. Bustreo, S. Ciattaglia, F. Cismondi, M. Coleman, V. Corato, C. Day, E. Diegele, U. Fischer, T. Franke, C. Gliss, A. Ibarra, R. Kembleton, A. Loving, F. Maviglia, B. Meszaros, G. Pintsuk, N. Taylor, M.Q. Tran, C. Vorpahl, R. Wenninger, J.H. You, DEMO design activity in Europe: progress and updates, Fusion Eng. Des. 136 (2018) 729–741, https://doi.org/10.1016/j.fusengdes.2018.04.001
[18] S.M. Gonzalez de Vicente, N.A. Smith, L. El-Guebaly, S. Ciattaglia, L. DiPace, M.R. Gilbert, R. Mandoki, S. Rosanvallon, Y. Someya, K. Tobita, D. Torcy, Overview on the management of radioactive waste from fusion facilities: ITER, demonstration machines and power plants, Nucl. Fusion 62 (2022) 085001, , https://doi.org/10.1088/1741-4326/ac62f7
[19] G.W. Bailey, O.V. Vilkhivskaya, M.R. Gilbert, Waste expectations of fusion steels under current waste repository criteria, Nucl. Fusion 61 (2021) 036010, , https://doi.org/10.1088/1741-4326/abc933
[20] M.R. Gilbert, T. Eade, T. Rey, R. Vale, C. Bachmann, U. Fischer, N. Taylor, Waste implications from minor impurities in European DEMO materials, Nucl. Fus. 59 (2019) 076015, , https://doi.org/10.1088/1741-4326/ab154e
[21] J.-Ch. Sublet, J.W. Eastwood, J.G. Morgan, M.R. Gilbert, M. Fleming, W. Arter, FISPACT-II: an advanced simulation system for activation, transmutation and material modelling, Nucl. Data Sheets 139 (2017) 77–137, https://doi.org/10.1016/j.nds.2017.01.002
[22] Koning, A.J., Rochman, D., Sublet, J. TENDL-2019; Release Date: December 31, 2019.Available from 〈https://tendl.web.psi.ch/tendl_2019/tendl2019.html〉.
[23] P.E. Blöchl, Projector augmented-wave method, Phys. Rev. B 50 (1994) 17953–17978, https://doi.org/10.1103/PhysRevB.50.17953
[24] G. Kresse, J. Furthmiiller, Efficient iterative schemes for ab initio total-energy calculations using a plane-wave basis set, Phys. Rev. B 54 (1996) 11169, https://doi.org/10.1103/PhysRevB.54.11169
[25] G. Kresse, J. Furthmiiller, Efficiency of ab-initio total energy calculations for metals and semiconductors using a plane-wave basis set, Comput. Mater. Sci. 6 (1996) 15–50, https://doi.org/10.1016/0927-0256(96)00008-0
[26] J. Hafner, Ab-initio simulations of materials using VASP: density-functional theory and beyond, J. Comput. Chem. 29 (2008) 2044–2078, https://doi.org/10.1002/jcc.21057
[27] J.P. Perdew, K. Burke, M. Ernzerhof, Generalized gradient approximation made simple, Phys. Rev. Lett. 77 (1997) 3865, https://doi.org/10.1103/PhysRevLett.77.3865
[28] H.J. Monkhorst, J.D. Pack, Special points for Brillouin-zone integrations, Phys. Rev. B 13 (1976) 5188, https://doi.org/10.1103/PhysRevB.13.5188
[29] B.E. Warren, X-ray Diffraction, Dover, New York, 1990.
[30] J.M. Cowley, An approximate theory of order in alloys, Phys. Rev. 77 (1950) 669, https://doi.org/10.1103/PhysRev.77.669
[31] A. Fernández-Caballero, M. Fedorov, J.S. Wróbel, P.M. Mummery, D. Nguyen-Manh, Configurational entropy in multicomponent alloys: matrix formulation from Ab initio based hamiltonian and application to the FCC Cr-Fe-Mn-Ni system, Entropy 21 (2019) 68, https://doi.org/10.3390/e21010068
[32] M. Fedorov, J.S. Wróbel, A. Fernadez-Caballero, K.J. Kurzydłowski, D. Nguyen-Manh, Phase stability and magnetic properties in fcc Fe-Cr-Mn-Ni alloys from first-principles modeling, Phys. Rev. B 101 (2020) 174416, , https://doi.org/10.1103/PhysRevB.101.174416
[33] A. Fernández-Caballero, J.S. Wróbel, P.M. Mummery, D. Nguyen-Manh, Short-range order in high entropy alloys: theoretical formulation and application to Mo-Nb-Ta-V-W system, J. Phase Equilibria Diffus. 38 (2017) 391–403, https://doi.org/10.1007/s11669-017-0582-3
[34] I. Mirebeau, M. Hennion, G. Parette, First measurement of short-range-order inversion as a function of concentration in a transition alloy, Phys. Rev. Lett. 53 (1984) 687–690, https://doi.org/10.1103/PhysRevLett.53.687